I&EC research
Industrial & Engineering Chemistry Research
pubs.acs.org/IECR
Article

Aluminous ZSM-48 Zeolite Synthesis Using a Hydroisomerization Intermediate Mimicking Allyltrimethylammonium Chloride as a Structure-Directing Agent

Miao Zhai,[‖] Hongxin Ding,[‖] Shu Zeng, Jiuxing Jiang, Shutao Xu, Xiujie Li,* Kake Zhu,* and Xinggui Zhou

Cite This: *Ind. Eng. Chem. Res.* 2020, 59, 11139−11148

Read Online

ACCESS | Metrics & More | Article Recommendations | Supporting Information

ABSTRACT: Manipulation of zeolite composition through judicious choice of an organic structure-directing agent (OSDA) is essential to regulate its physicochemical properties. ZSM-48 is a unidimensional zeolite that often crystallizes into siliceous form, and direct synthesis of the aluminous counterpart using low-cost OSDAs is thus far a bottleneck that has obstructed its deployment in large-scale implementation. This work shows the use of a specific OSDA, allyltrimethylammonium chloride, which structurally mimics the *iso*-alkyl carbenium ion intermediate found in *n*-heptane skeletal isomerization, is capable of producing aluminous ZSM-48 with more accessible protonic sites. The specificity of this OSDA is ascribed to the good match of its molecular size and shape to the microchannel geometry of the structure and its rigidity endowed by the presence of the $CH{=}CH_2$ moiety. The obtained material (a Si/Al ratio of ca. 23.0) possesses more medium-to-strong Bronsted acid sites (by a factor of 1.36) and enhanced diffusion property (12 times) with respect to a control sample (Si/Al of ca. 26.7) derived from an expensive, often used OSDA, pentamethonium bromide, as evidenced by NH_3-IR spectroscopy and gravimetric adsorption uptake measurement using 2-methylhexane as a probe molecule, respectively. The difference in acid site density between the two samples can be ascribed to the influences of OSDA on crystallinity, amount of Al incorporation, and associated Al sitting. A significant increase in isomer yield from 44 to 72% in *n*-heptane hydroisomerization has been attained using the obtained ZSM-48 as an acid catalyst with respect to the control sample.

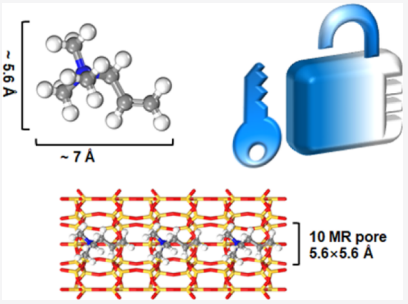

1. INTRODUCTION

Zeolites are a family of crystalline microporous (<2 nm) materials whose framework is made up of tetrahedral TO_4 (T = Si, Al, etc.) units that are spatially interconnected through a corner-sharing O vertex.[1−3] As molecular sieve materials, zeolites find widespread applications as heterogeneous catalysts, adsorbents, ion-exchangers, hosts of accommodated guests, etc., and new applications are frequently reported.[4,5] Apart from discovering new framework topologies, broadening framework composition is a profitable strategy to tune their physicochemical properties and widen their application fields, henceforth, is an important target of zeolite synthesis.[6,7] For instance, the recently developed organic structure-directing agents (OSDAs) have enabled the synthesis of a high silicon **LTA** zeolite (Si/Al ratios from 10, up to infinity) and expanded its use from adsorbents, desiccants, and ion-exchangers to methanol-to-olefin (MTO) and NH_3-selective catalytic reduction (NH_3-SCR) catalysts.[7−9] On the other hand, Corma et al.[10] have recently proposed the use of molecules mimicking the transition states or reaction intermediates of pre-established catalytic reactions as OSDAs to generate more active and selective catalysts, that is, ITQ-27 for toluene disproportionation,[10] ITQ-64 for ethylbenzene isomerization,[10] MIT-1 for adamantane synthesis,[10] and RUB-13, SAPO-18, and SSZ-13 for MTO.[11] Herein, this work demonstrates that the use of a reaction intermediate mimicking molecule as an OSDA is also a promising way to expand the framework composition and control the Al sitting of zeolites.

ZSM-48 possesses a ***MRE** topology and a unidimensional cyclic shaped pore (5.6 × 5.6 Å) delimited by 10-membered rings.[12,13] Until now, two generic types of OSDAs, that is, amines and quaternary ammonium cations (as summarized from the literature survey in Table S1 of the Supporting Information), have been used to crystallize ZSM-48. Only siliceous ZSM-48 (often Si/Al > 100) could be produced using amines. On the other hand, diquaternary ammonium cations could direct the formation of varied crystalline phases (i.e., competing **EUO**, **MWW**, or **MTW**) relying on the identity, concentration of alkali metals, or Si/Al ratios in the initial gels, owing to the flexible nature of alkyl chains that link the

Received: February 13, 2020
Revised: April 14, 2020
Accepted: May 22, 2020
Published: May 22, 2020

https://dx.doi.org/10.1021/acs.iecr.0c00750
Ind. Eng. Chem. Res. 2020, 59, 11139−11148

Scheme 1. Illustration of Simplified *n*-Heptane Hydroisomerization Mechanism, *n*-Heptane Dehydrogenation to *n*-Heptenes over Pt That Are Further Protonated on Acid Sites, Whereafter They Proceed Further Skeletal Isomerization To Form Various *iso*-Alkyl Cations (Including 2-Methylhexane, Denoted in Red) before Being Hydrogenated to Products (a)[a]

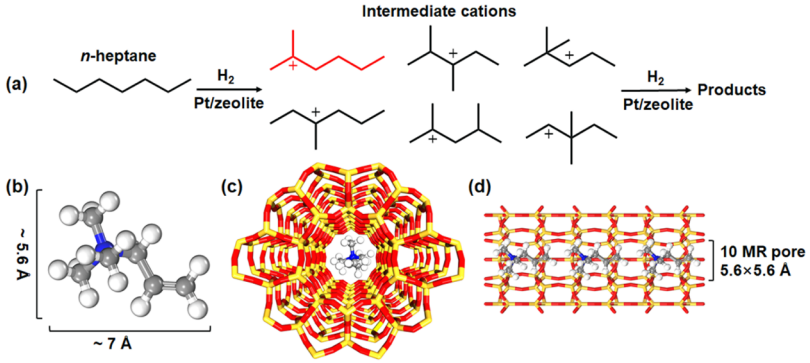

[a]The cation $ATMA^+$ mimics 2-methylhexyl ion as it possesses one less carbon atom in the alkyl chain, but one more methyl group in the cationic moiety, and is used to crystallize ZSM-48 (b). Structure of ZSM-48 with occluded $ATMA^+$ along the pore axis (c) and perpendicular to the pore axis (d).

diquaternary cations.[14] Thus far, the only feasible way to generate highly crystalline ZSM-48 with a Si/Al ratio of 30 is to use diquaternary cationic pentamethonium bromide ($PMBr_2$, $(CH_3)_3N^+(CH_2)_5N^+(CH_3)_3$) as an OSDA,[14] which, however, involves a complex preparation and is prohibitively expensive for industrial use. In addition, the obtained material suffers from low Bronsted acid site (BAS) density (vide infra), suggesting a low efficiency in catalysis. Recently, the use of $(C_{22}H_{45}N^+(CH_3)_2C_6H_{12}N^+(CH_3)_2CH_2C_6H_4CH_2N^+(CH_3)_2C_6H_{12}N^+(CH_3)_2C_{22}H_{45})(Br^-)_2(Cl^-)_2$ as an OSDA to generate ZSM-48 with a Si/Al ratio of 31 has been reported, but low crystallinity, presence of competing phases, and expensive preparation for OSDA remain problematic for its practical use.[15] As an acid catalyst, ZSM-48, along with other unidimensional zeolites, such as commercialized ZSM-22[16−18] and ZSM-23,[19−21] is suitable for industrially relevant hydroisomerization, a critical process for promoting the cold flow properties of fuels and lubricants.[22,23] Besides, other applications in catalytic hydrocracking and hydroisomerization of *n*-alkanes,[24,25] isopropylation of benzene,[26] methanol-to-hydrocarbon conversion,[27] and so on, are also known. Despite of the postsynthetic desilication protocol recently developed[28] and aforementioned efforts, a cost-effective way to manufacture aluminous ZSM-48 using a commercially available OSDA, a long-standing technological bottleneck, is yet to be addressed.

This work sought a solution by resorting to the intended reaction to be catalyzed, as inspired by the use of reaction intermediate or transition state mimicking molecules as OSDAs.[10,11] According to previously established reaction mechanism and kinetics,[29−31] hydroisomerization of *n*-heptane proceeds through consecutive steps involving dehydrogenation to heptenes, their protonation to from *n*-heptyl ions, and subsequent skeletal rearrangement into *iso*-heptyl ions, followed by deprotonation and hydrogenation to produce various isomers, as displayed in Scheme 1a. *Iso*-heptyl ions are recognized as the most abundant surface intermediate and play key roles in this transformation.[31] Allyltrimethylammonium chloride ($ATMA^+$) was selected as an OSDA to crystallize aluminous ZSM-48, for its analogous structure and size to carbenium ion intermediate 2-methylhexyl ion (Scheme 1b), which also has the same size as that of micropores found in ZSM-48, (Scheme 1c,d). For comparison, trimethylpropylammonium ($TMPA^+$) bromide, another reaction intermediate mimicking OSDA, was also attempted. The acidity and catalytic properties of the obtained material was assessed in *n*-heptane hydroisomerization and compared with a sample of close Si/Al ratio derived from $PMBr_2$.

2. EXPERIMENTAL SECTION

2.1. Sample Preparation. ZSM-48-ATMA was prepared using a conventional hydrothermal route. The molar composition of the starting gel was $30SiO_2/0.5Al_2O_3/9.0ATMA^+/4.0Na_2O/1200H_2O$. In a typical synthesis, 0.38 g of aluminum nitrate nonahydrate ($Al(NO_3)_3{\cdot}9H_2O$, ≥ 99%, Shanghai Macklin Biochemical Reagent Co. Ltd.) was dissolved in 16.97 g of deionized water before adding 0.33 g of sodium hydroxide (NaOH, ≥ 96%, Shanghai Titan Scientific Co. Ltd.) and 1.25 g of allyltrimethylammonium chloride ($ATMA^+$, 98%, Shanghai Macklin Biochemical Reagent Co. Ltd.) to form a solution. After homogenizing by stirring for 15 min, 6.44 g of tetraethyl orthosilicate (TEOS, ≥ 28% SiO_2, Shanghai Titan Scientific Co. Ltd.) was charged, and the mixture was further stirred for 5 h. The resultant mixture was sealed into a 100 mL Teflon autoclave and hydrothermally crystallized at 433 K for 48 h under tumbling condition (80 rpm). The solid product was recovered through centrifugation and washed before being dried at 353 K for 10 h, and subsequently calcined at 823 K for 10 h to remove the OSDA. The calcined sample was ion-exchanged five times with NH_4Cl (1 $mol{\cdot}L^{-1}$) to its NH_4^+− form at 353 K under refluxing for 8 h each time, accompanied by vigorously stirring. The proton form sample, HZSM-48-ATMA, with the suffix ATMA standing for allyltrimethylammonium chloride, was produced after calcinations. ZSM-48-ATMA samples with varied Si/Al ratios were synthesized by manipulating the amount of $Al(NO_3)_3{\cdot}9H_2O$ used under otherwise identical conditions.

ZSM-48-TMPA (the suffix TMPA stands for $TMPA^+$) was synthesized using trimethylpropylammonium bromide ($TMPA^+$, 99%, Shanghai Meryer Chemical Technology Co., Ltd) as an OSDA. Synthesis of ZSM-48-TMPA samples with other Si/Al ratios was also conducted and processed under identical conditions as described for ZSM-48-ATMA.

https://dx.doi.org/10.1021/acs.iecr.0c00750
Ind. Eng. Chem. Res. 2020, 59, 11139−11148

For comparison, ZSM-48-PMB was synthesized hydrothermally with homemade $PMBr_2$ as an OSDA according to the literature method.[27] In brief, 39.80 mL of trimethylamine (TMA, 33 wt % in ethanol, Alfa Aesar Chemicals Co. Ltd.) was mixed with 75 mL of ethanol, followed by adding 9.20 mL of 1,5-dibromopentane (DBP, 98%, TCI Development Co. Ltd.) (TMA/DBP = 2.5:1), and the mixture was refluxed for 24 h at an ambient temperature, thereafter filtered, and dried at 343 K under vacuum (^{13}C NMR spectra of $PMBr_2$, as displayed in Figure S1 of the Supporting Information). The molar composition of the starting gel of ZSM-48-PMB was $30SiO_2/0.5Al_2O_3/4.5PMBr_2/5.0Na_2O/1200H_2O$, with respect to the reported procedure.[27] Specifically, 0.38 g of $Al(NO_3)_3 \cdot 9H_2O$, 0.42 g of NaOH, and 1.57 g of $PMBr_2$ were dissolved in 16.97 g of deionized water. Next, 6.44 g of TEOS was added dropwise and homogenized via stirring for 5 h. Finally, the resultant mixture was enclosed into a 100 mL Teflon autoclave, followed by hydrothermal crystallization under tumbling (80 rpm) at 433 K for 168 h. The product was processed using the same manipulations as mentioned above, with the attained sample named HZSM-48-PMB, whereby the suffix PMB stands for $PMBr_2$.

Bifunctional catalysts, such as Pt/HZSM-48 with 0.5 wt % Pt, were prepared using the solution impregnation method with a specific step completely consistent with our previous work.[32] The final catalysts were labeled Pt/HZSM-48-ATMA and Pt/HZSM-48-PMB.

2.2. Characterization. X-ray diffraction (XRD) patterns were gathered using a Rigaku D/Max 2550 VB/PC diffractometer, operated at 40 kV and 100 mA with the Cu Kα X-ray source (λ = 1.5418 Å). A scanning rate of 10° min^{-1} was adopted in the 2θ range from 5 to 50°. Field emission scanning electron micrographs and transmission electron micrographs were captured on a NOVA Nano SEM 450 (FEI) and a JEM-2011 (JEOL), respectively. The N_2 adsorption−desorption isotherms were measured on an ASAP 2020 analyzer at 77 K. The samples were outgassed under vacuum at 623 K for 24 h to remove impurities before collecting the N_2 physisorption data. Both the Brunauer−Emmett−Teller (BET) and Langmuir methods were used to analyze the sample surface areas. The *t*-plot method was employed to generate micropore volumes. Thermogravimetric analysis (TGA) was operated on a thermogravimetric analyzer Pyris 1 TGA setup under air atmosphere. All samples were heated to 1073 K from room temperature at a rate of 5 K·min^{-1}. Pyridine infrared spectroscopy (Py-IR) was performed to measure the acidity of all samples using a Spectrum 100 Fourier transform infrared spectrometer. The samples to be tested were loaded into self-supporting wafers and pretreated for 3 h at 673 K under vacuum to remove impurities. The number of absorbed pyridine molecules was quantified using the molar extinction coefficients [$\varepsilon_{Bronsted}$(1545 cm^{-1}) = 1.67 cm·$\mu$$mol^{-1}$ and ε_{Lewis}(1455 cm^{-1}) = 2.22 cm·$\mu$$mol^{-1}$][33] to the integrated area of the corresponding bands. NH_3 infrared spectroscopy (NH_3-IR) was performed to quantify the total number of acid sites referring to the corresponding molar extinction coefficients [$\varepsilon_{Bronsted}$(1450 cm^{-1}) = 1.47 cm·$\mu$$mol^{-1}$ and ε_{Lewis}(1630 cm^{-1}) = 1.98 cm·$\mu$$mol^{-1}$].[34,35] All samples were pretreated under the same condition as for Py-IR measurements. Inductively coupled plasma atomic emission spectrometry (ICP−AES) was utilized for elementary analysis, which was carried out on an IRIS 1000. The Pt dispersion on Pt/HZSM-48 was identified using H_2 chemisorption on a Micromeritics Autochem 2920. Solid-state magic-angle spinning nuclear magnetic resonance (MAS NMR) was implemented using a 14.1 T Bruker AVANCE-III spectrometer operating at a ^1H Larmor frequency of 600 MHz. Sample preparation and data collection details were described in detail in a recent article by some of us.[36] The deconvolution of one-dimensional (1D) ^{27}Al MAS NMR spectra was derived from the DMFIT program, where the quadrupolar line shape fitting was used. The chemical shifts of ^{13}C and ^{29}Si were based on tetramethylsilane, while the chemical shifts of ^{27}Al were based on aluminum nitrate (1.0 wt % in water).

2.3. Diffusivity Property Measurements. The diffusion properties in ZSM-48 crystals were studied using gravimetry on an intelligent gravimetric analyzer instrument (IGA-100), following a reported procedure described in our previous article,[32] using 2-methylhexane (2-MC_6) as a probe molecule. The effective diffusion coefficient is determined by Fick's second law, representing the change in the concentration of the adsorbate inside the porous slab of the adsorbent (assuming an infinite extension in the lateral direction)

$$\frac{\partial C}{\partial t} = D_{eff}\left(\frac{\partial^2 C}{\partial x^2}\right) \tag{1}$$

In eq 1, D_{eff} is the diffusion coefficient, C is the 2-MC_6 concentration inside the slab, x is the distance to the center of the slab, and t being the time at the initial stage of uptake in an adsorption process.

When the adsorption process begins on the slablike crystals, the solution of the above equation can be approximated as follows

$$\frac{q(t)}{q(\infty)} = \frac{2}{\sqrt{\pi}}\sqrt{\frac{D_{eff}}{L^2}}\sqrt{t} \tag{2}$$

In eq 2, L is the characteristic diffusion length of the crystal and $q(t)/q(\infty)$ is the normalized 2-MC_6 adsorption. Because of the anisotropic diffusion of molecules in unidimensional pores of the ***MRE** structure along the *a*-axis, the slab model is appropriate, as also used previously by Choi et al.[37] for unidimensional zeolites.

2.4. Catalytic Performance Evaluations. The catalytic performance of catalysts in *n*-heptane (C_7) hydroisomerization was evaluated using a fixed-bed reactor loading 0.4 g of the bifunctional catalyst Pt/HZSM-48 (20−40 mesh) at a continuous flow and atmospheric pressure under a specific reaction condition, weight hourly space velocity = 0.5 $g_{n\text{-heptane}} \cdot (g_{cat} \cdot h)^{-1}$, and n_{H_2/C_7} = 26, referring to our previous work[32] for the details.

2.5. Computations. The structural optimization was conducted using Density Functional Theory (DFT, Perdew−Burke−Ernzerhof, 96T Periodic Model, ZSM-48 (polymorph 6) zeolite crystallography data from International Zeolite Association database) calculations for further lattice energy minimization of aluminous ZSM-48 zeolite. The site of Al substitution was allowed to relax, while other silicon sites were fixed to the specific crystallographic sites, and the optimized structure after calculation was used to estimate the NMR resonance peaks using −Al−O−Si− bond angles thus obtained with eq 3. Based on the comparative analysis of crystallographic and ^{27}Al MAS NMR data of aluminous zeolites, Lippmaa et al.[38,39] proposed a generally applicable, semi-empirical correlation (eq 3) between the ^{27}Al MAS NMR

https://dx.doi.org/10.1021/acs.iecr.0c00750
Ind. Eng. Chem. Res. 2020, 59, 11139−11148

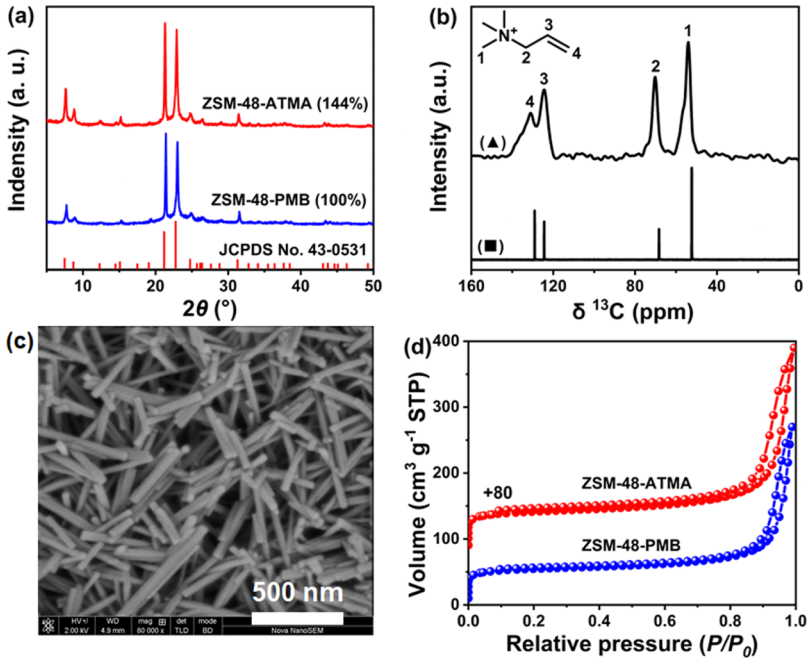

Figure 1. XRD patterns of ZSM-48-PMB and ZSM-48-ATMA (a) and relative crystallinity (inset of a). (▲) $^{1}H-^{13}C$ CP MAS NMR spectra of ZSM-48-ATMA with $ATMA^{+}$ occluded in the pores and (■) ^{13}C NMR spectra of $ATMA^{+}$ in D_2O solution (b). Field emission scanning electron micrograph micrograph of ZSM-48-ATMA (c). N_2 physisorption isotherms of ZSM-48-PMB and ZSM-48-ATMA (d).

Table 1. Textural Properties of Calcined ZSM-48-PMB and ZSM-48-ATMA, Pt Dispersion on Bifunctional Catalysts, Diffusion Time Constant Value D_{eff}/L^2 Calculated Derived from Figure 5, Si/Al Ratios, and Yield of ZSM-48 Crystals

sample	Si/Al[a]	S_{BET} ($m^2 \cdot g^{-1}$)[b]	$S_{Langmuir}$ ($m^2 \cdot g^{-1}$)[c]	V_{micro} ($cm^3 \cdot g^{-1}$)[d]	Pt dispersion (%) (Pt/H^+)[e]	D_{eff}/L^2 (s^{-1})	yield (%)[f]
ZSM-48-PMB	26.7	203	236	0.06	16.2 (1.15)	2.39×10^{-4}	84.7
ZSM-48-ATMA	23.0	208	289	0.07	45.8 (0.85)	2.91×10^{-3}	83.3

[a]Determined by ICP−AES. [b]Calculated by the BET method. [c]Calculated by the Langmuir method. [d]Deduced by the *t*-plot method. [e]Determined by H_2 chemisorption after loading 0.5 wt % Pt. [f]Calculated by weight method.

isotropic chemical shift δ_{iso} (in ppm) and the average −Al−O−Si− bond angle θ for a given T sites

$$\delta_{iso} = -0.5\theta + 132 \quad (3)$$

3. RESULTS AND DISCUSSION

The phase compositions of ZSM-48-ATMA and ZSM-48-PMB were inspected through XRD technique, as exhibited in Figure 1a. No reflections other than those from the ***MRE** structure (JCPDS No. 43-0531) were determined, neither is non-converted raw materials found. Noteworthily, ZSM-48 is not a code for one crystal structure, but for a family of materials with similar but not identical structures, which often causes broadening of diffraction lines between 2θ of 20−25°, as a result of formation of intergrown polymorphs or presence of stacking faults.[13] The pattern of ZSM-48-ATMA is close to the simulated polymorph 6.[13] A relative crystallinity of 144% could be deduced for ZSM-48-ATMA by taking ZSM-48-PMB (100%) as a reference. The higher relative crystallinity underlines that $ATMA^{+}$ is better suited toward the crystallization of ZSM-48 than $PMBr_2$. The TGA curves of as-synthesized samples show that the initial decomposition temperature of occluded OSDA for ZSM-48-ATMA is about 100 K lower than that of ZSM-48-PMB (Figure S2), suggesting a less detrimental effect of calcination process to framework integrity. The yield of ZSM-48-ATMA product was 83.3% on an inorganic basis, which was close to that of ZSM-48-PMB (84.7%). Nominal Si/Al ratios of ca. 23.0 and 26.7 were obtained by elemental analyses, for ZSM-48-ATMA and ZSM-48-PMB, respectively (Table 1). To explore the full potential of $ATMA^{+}$ as an OSDA, ZSM-48-ATMA with varied Si/Al ratios were also synthesized. The corresponding XRD patterns are shown in Figure S3, demonstrating that $ATMA^{+}$ is applicable for Si/Al ratio variations spanning from 30 to 300, indicating the high specificity of $ATMA^{+}$. This high specificity toward ***MRE** topology is advantageous over the expensive $PMBr_2$, as the latter readily induces the formation of competing phases like zeolite with **EUO** topology at low Si/Al ratios.[14]

To prove that it was $ATMA^{+}$ instead of the decomposed molecule that acted as an OSDA in the hydrothermal synthesis, the $^{1}H-^{13}C$ CP MAS NMR spectra of as-synthesized ZSM-48-ATMA with occluded $ATMA^{+}$ were collected (Figure 1b). The signals with chemical shifts at 54, 70, 125, and 131 ppm in the $^{1}H-^{13}C$ CP MAS NMR spectra are attributed to four types of structures, that is, $-(CH_3)_3$, $-CH_2-$, $-CH=$, and $-CH=CH_2$, respectively, which are essentially the same as $ATMA^{+}$ dissolved in D_2O. Elemental analysis shows that the as-synthesized sample contains 4.53 wt % C, 0.89 wt % N, which is consistent with the chemical formula of $ATMA^{+}$. From these, one may conclude that $ATMA^{+}$ retained intact during the hydrothermal synthesis. The role of carbon−carbon double bond is thus far not well understood, but a control sample generated by replacing $ATMA^{+}$ with $TMPA^{+}$ as an OSDA

https://dx.doi.org/10.1021/acs.iecr.0c00750
Ind. Eng. Chem. Res. 2020, 59, 11139−11148

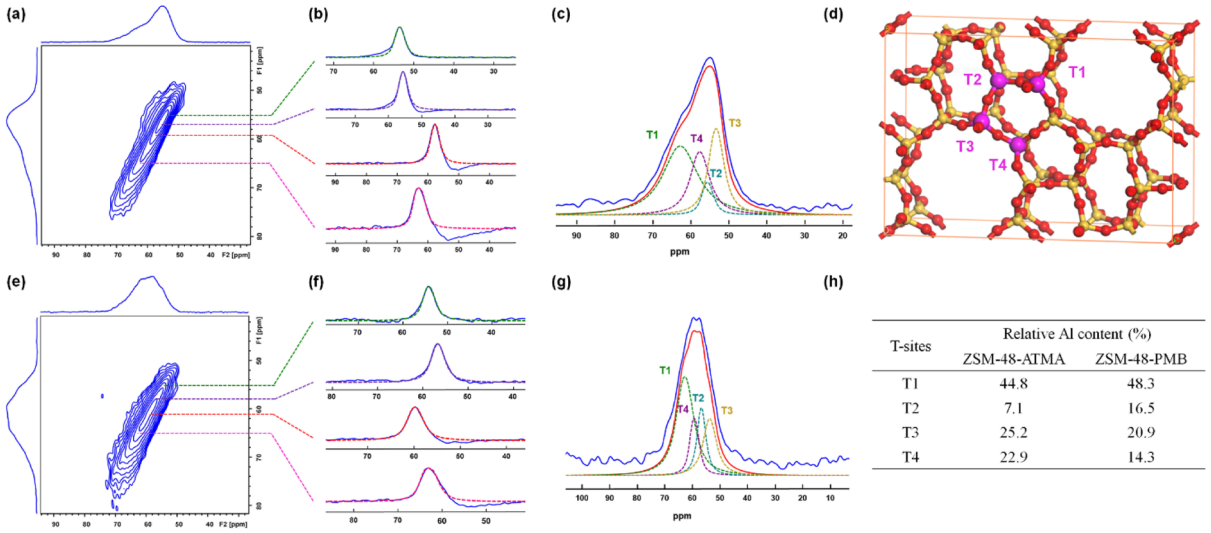

T-sites	Relative Al content (%)	
	ZSM-48-ATMA	ZSM-48-PMB
T1	44.8	48.3
T2	7.1	16.5
T3	25.2	20.9
T4	22.9	14.3

Figure 2. 2D ^{27}Al 3Q MAS NMR spectra with their isotropic projections and 1D single-pulse ^{27}Al NMR spectra with their fitting curves for ZSM-48-ATMA (a–c) and ZSM-48-PMB (e–g). Schematic diagram of the ZSM-48 crystal structure (polymorph 6) and T sites taken up by Al atoms are represented in purple color (d). Relative Al content at each T site in ZSM-48, with respect to the relative Al content of the fitting peaks in the F1 spectrum for each T site (h).

under otherwise identical conditions gives ZSM-48 (Si/Al = 30) together with mordenite as an impurity phase (Figure S4), implying that the presence of $-CH{=}CH_2$ plays a critical role for a successful synthesis. It is likely a result of molecule rigidity change by the presence of $-CH{=}CH_2$. As $TMPA^+$ is structurally more close to the reaction intermediate 2-methylhexyl ion, attempts were also made to generate ZSM-48 with a broader composition range. It was found to be possible to fabricate pure-phase ZSM-48 only at a narrow synthetic window for a Si/Al ratio at ca. 70 (Figure S4) to avoid the formation of impurities. One may therefore conclude that $ATMA^+$ is a better suited OSDA than $TMPA^+$, and a broader composition is only attainable by employing it.

The field emission scanning electron micrograph shown in Figure 1c discloses that ZSM-48-ATMA is composed of uniform, discrete needle-shaped crystals, and the length of crystals ranges from 0.3 to 1.0 μm with a diameter of ca. 50 nm, showing a typical morphology of unidimensional zeolites. An average aspect ratio of 12 could be inferred. In contrast, ZSM-48-PMB is made up of treelike crystals with rod-shaped crystals and branching thinner ones (1–2 μm in length and ca. 70 nm across), implying a twinning growth rich in grain boundaries. In addition, some assembled sheetlike crystals could also be visualized (Figure S5). The morphology is essentially the same as previously reported.[27] ZSM-48 derived from $ATMA^+$ with other Si/Al ratios are shown in Figure S6, and the needle-shaped crystals gradually become thicker with increasing Si/Al ratios up to 300. The transmission electron micrographs further corroborate the observation, and the lattice fringes are clearly visible (Figure S7).

The textural properties of calcined samples were obtained using N_2 physisorption isotherms, as outlined in Figure 1d. The detailed data are compiled in Table 1. The N_2 adsorption–desorption isotherm of ZSM-48-ATMA displays a typical type I curve, which is ascribed to the micropore filling process at $P/P_0 < 0.01$. The micropore volume and Langmuir and BET surface areas of calcined ZSM-48-ATMA are 0.07 $cm^3{\cdot}g^{-1}$, 289 $m^2{\cdot}g^{-1}$, and 208 $m^2{\cdot}g^{-1}$, respectively, which are comparable to that of ZSM-48-PMB (0.06 $cm^3{\cdot}g^{-1}$, 236 $m^2{\cdot}g^{-1}$, and 203 $m^2{\cdot}g^{-1}$) and the reported value (BET, surface area of 219 $m^2{\cdot}g^{-1}$).[27] Unidimensional zeolites normally have a relatively low surface area and micropore volume with respect to their three-dimensional counterparts.

Solid-state NMR, as a powerful technique to determine the chemical environment for component incorporation in zeolite framework, could be used to provide structural information of atom incorporation. The ^{27}Al MAS NMR spectra (Figure S8) for calcined ZSM-48-ATMA and ZSM-48-PMB show that both samples have only one envelope resonance peak centered at ca. 56 ppm, attributable to the typical tetrahedral coordination Al species.[40] Extraframework Al at 0 ppm with octahedral coordination was not detected. Nevertheless, it has been difficult to distinguish the Al sitting in the ZSM-48 framework in the nonequivalent tetrahedral position by ^{27}Al MAS NMR because of the strong quadrupolar effect of Al.

For this reason, the two-dimensional (2D) ^{27}Al 3Q MAS NMR spectra were also collected in order to probe distribution of Al atoms on the four distinct crystallographic sites (Figure 2a,e). 1D slices of the isotropic projection along with F1 direction (reflecting distribution of chemical shift) extracted from the 2D 3Q MAS NMR (Figure 2b,f) were used to estimate the Al resonance peaks according to the crystal structure of polymorph 6 (Figure 2d). Note that the connectivity of T-atoms in all polymorphs and their intergrowths is the same according to the structural model postulated by Lobo and van Koningsveld.[13] Al sitting is regarded to be invariant among the intergrown structures. The obtained quadrupolar parameters are presented in Table S2. The chemical shift of Al locating at each T-site was calculated using eq 3, which correlates the chemical shift to the T–O–T bond angle (as shown in Table S3), based on the crystal model.[13,38] The majority of Al atoms in ZSM-48-ATMA were found to be situated at the T1 site (44.8%), followed by T3 (25.2%), T4 (22.9%), and T2 (7.1%) sites (Figure 2c, h). In ZSM-48-PMB, more Al occupation on T1 (48.3%) sites was measured, followed by T3 (20.9%) and T4 (14.3%) sites, but a relatively high proportion of T2 (16.5%) was determined (Figure 2g,h). Among these sites, the T2 site is not accessible

https://dx.doi.org/10.1021/acs.iecr.0c00750
Ind. Eng. Chem. Res. 2020, 59, 11139–11148

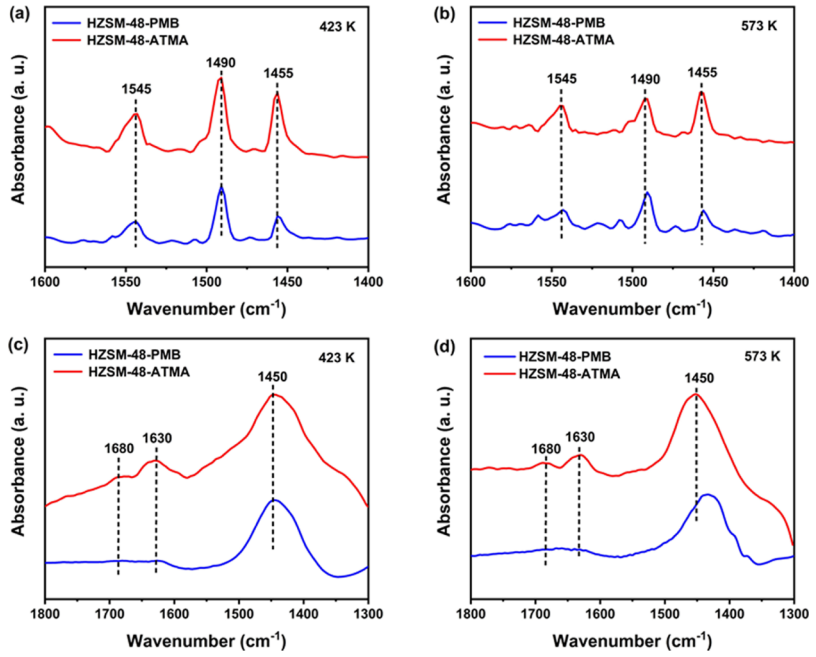

Figure 3. Acidic properties of ZSM-48-PMB and ZSM-48-ATMA measured by pyridine desorption IR (a,b) and NH_3 desorption IR (c,d).

Table 2. Acid Strength and Density Distribution in HZSM-48-PMB and HZSM-48-ATMA Samples

	$C_{B,Py}$ (μmol·g^{-1})[a]		$C_{L,Py}$ (μmol·g^{-1})[a]		C_{B,NH_3} (μmol·g^{-1})[b]		C_{L,NH_3} (μmol·g^{-1})[b]	
sample	423 K	573 K	423 K	573 K	423 K	573 K	423 K	573 K
ZSM-48-PMB	20	18	13	10	369	221	35	19
ZSM-48-ATMA	41	30	30	26	440	300	79	47

[a]Calculated by pyridine desorption IR. [b]Calculated by NH_3 desorption IR.

from the 10-membered ring channels and is regarded unimportant for the generation of accessible protonic sites. The ^{29}Si MAS NMR spectra (Figure S9) for calcined ZSM-48-ATMA and ZSM-48-PMB display a major signal with chemical shifts of −113 ppm, assignable to the Si(4Si,0Al) environment, which is common for high silicon zeolites.[41] Therefore, the preferential sitting of more Al atoms on accessible sites in ZSM-48-ATMA, together with the high crystallinity, recommends more strong and accessible BAS.

To evaluate the acid strength and density, Py-IR was first used for the qualitative and quantitative evaluation of acidity. The vibration band at 1545 cm^{-1} is assignable to the generation of pyridinium ions on BAS, among which the vibration band at 1455 cm^{-1} is related to Lewis acid sites (LAS), while the vibration band at 1490 cm^{-1} results from the joint contribution from both types of acid sites (Figure 3a,b).[33] The corresponding amounts for total and medium-to-strong acid sites were calculated using the Py-IR data from desorption at 423 and 573 K, respectively, as summarized in Table 2. It could be found that HZSM-48-ATMA has more BAS compared to HZSM-48-PMB. Notably, the determined acid sites with pyridine as a probe are far less than the amount that can be expected from the aluminum content detected by ICP−AES, indicating that pyridine as a probe could not detect all acid sites locating in the micropores of ZSM-48. Because of the small pore size and the long 1D channels of ZSM-48 crystals, the relatively large kinetic diameter of pyridine molecule (5.7 Å)[42] could limit its entry into the micropores (ca. 5.6 Å) or block micropore channels for transport of other pyridine molecules. Therefore, Py-IR can only detect the amount of acid sites accessible by pyridine through external surfaces.

In order to get more precise BAS and LAS information, NH_3-IR was complementarily performed (as depicted in Figure 3c,d). The NH_3-IR data for desorption at 423 K were utilized to estimate the amount of total acid sites, while medium-to-strong acid sites were deduced from the data collected at 573 K, as summarized in Table 2. Because the kinetic diameter of ammonia (2.6 Å) is markedly smaller than the micropore dimension of ZSM-48, all acid sites inside the micropores are supposed to be accessible by NH_3. The vibration bands at 1450 and 1680 cm^{-1} are assigned to the formation of ammonium ions on BAS and that the 1630 cm^{-1} vibration band is due to ammonia coordinated to LAS.[34,35] The BAS density of HZSM-48-ATMA (440 and 300 μmol·g^{-1}, measured as 423 and 573 K, respectively) is much larger than that of HZSM-48-PMB (369 and 221 μmol·g^{-1}, measured as 423 and 573 K, respectively) (Table 2). The difference in acid site density between the two samples can be ascribed to a combined influence out of crystallinity (144 *vs.* 100%, for ZSM-48-ATMA and ZSM-48-PMB), Al incorporation content (Si/Al ratio, 23.0 vs 26.7, for ZSM-48-ATMA and ZSM-48-PMB), and sitting (less T2 site occupation in ZSM-48-ATMA with respect to ZSM-48-PMB, i.e., 7.1 vs 16.5%), which, in turn, are dictated by the choice of the OSDA. Among them, the amounts of BAS with medium-to-strong strength are generally regarded to be catalytically important, which have been amplified (by 1.36 times) by using ATMA$^+$ as the OSDA.

The HZSM-48 zeolite as an acid component was loaded with 0.5 wt % Pt to afford bifunctional catalysts and evaluated

https://dx.doi.org/10.1021/acs.iecr.0c00750
Ind. Eng. Chem. Res. 2020, 59, 11139−11148

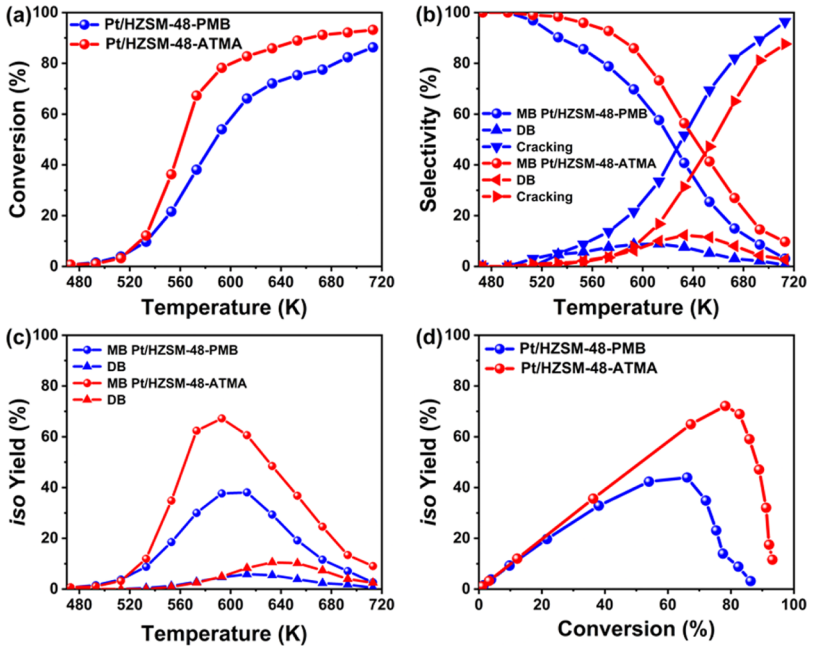

Figure 4. Reactant conversion (a), product selectivity (b), yield isomer to MBs and DBs (c) vs reaction temperature (473−713 K), and total isomer yield versus reactant conversion (d) in *n*-heptane hydroisomerization.

in *n*-heptane hydroisomerization, in order to verify the design concept and evaluate the catalytic property. For bifunctional catalysts, the balance of Pt sites and acid sites is crucial for their catalytic performance. It has been shown that when the Pt/H^+ ratio is above 0.03 (ideal operation condition), it is secure that (de)hydrogenation process is equilibrated such that the catalytic performance relies solely on the acid component of bifunctional catalysts.[30,43] The Pt/H^+ ratios of Pt/HZSM-48-PMB (1.15) and Pt/HZSM-48-ATMA (0.85) were derived from chemisorption of H_2 and acid sites measured from NH_3-IR at 573 K, as displayed in Table 1, which suffice that the requirement of ideal operation condition and catalytic performance is therefore dictated by zeolite and is independent of Pt site function. Catalytic activity in *n*-heptane hydroisomerization increases faster with temperature rise for Pt/HZSM-48-ATMA than Pt/HZSM-48-PMB from 473 to 613 K (for Pt/HZSM-48-ATMA) or 633 K (for Pt/HZSM-48-PMB) (Figure 4a). Correlating with the results of acidity measurement, it can be inferred that the Pt/HZSM-48-ATMA catalyst shows higher catalytic activity as a result of increased medium-to-strong acid site density, as the process is operating in a kinetic controlled regime at low temperatures (before reaching a maximum isomer yield).[44,45] At higher temperatures, the high conversion of Pt/HZSM-48-ATMA is ascribed mainly to the enhancement of diffusion properties, as the reaction enters the diffusion-controlled regime at an elevated temperature region when cracking reaction dominates.[31] The monomethyl-branched isomers (MBs, 2-methylhexane, 3-methylhexane, and 3-ethylpentane; $2\text{-}MC_6$, $3\text{-}MC_6$, and $3\text{-}EC_5$, respectively), dimethylbranched isomers (DBs, i.e., 2,3-dimethylpentane ($2,3\text{-}DMC_5$), $2,4\text{-}DMC_5$, $2,2\text{-}DMC_5$, and $3,3\text{-}DMC_5$), and cracking selectivity versus reaction temperature curves are plotted in Figure 4b. MBs decrease monotonically with increasing temperature. Pt/HZSM-48-ATMA exhibits significantly higher MB selectivity than that of Pt/HZSM-48-PMB, suggesting a shortened residence time. MBs are further transformed into DBs with increasing temperature, at high conversion levels, as a result of consecutive skeletal isomerization reaction.[31] The maximum selectivity for DBs is reached at temperatures of 613 and 633 K for Pt/HZSM-48-PMB (8.9%) and Pt/HZSM-48-ATMA (12.3%), respectively. At higher temperatures, in particular, in the diffusion-controlled regime, DBs undergo cracking into smaller molecules, giving rise to a lowered isomer selectivity, as shown by a volcano curve in Figure 4c. The isomer selectivity has been revealed to reflect the diffusion property of the acid support[44,46] and the high isomer selectivity, therefore suggesting a shortened residence time of DBs within the micropores. The reduction of residence often suggests a lower probability of unwanted cracking reaction and is an indication of better diffusion property of ZSM-48-ATMA. To certify this, diffusion measurements using 2-methylhexane as a probe molecule were conducted, as displayed in Figure 5, where the results showed that an increase in D_{eff}/L^2 by a factor of 12 times for ZSM-48-ATMA with respect to ZSM-48-PMB could be inferred (Table 1). Given the identical micropore size, it is reasoned that the difference in diffusion property mainly originates from the effective diffusion length, that is, *L*. Comparisons of morphological features between the two samples, that is,

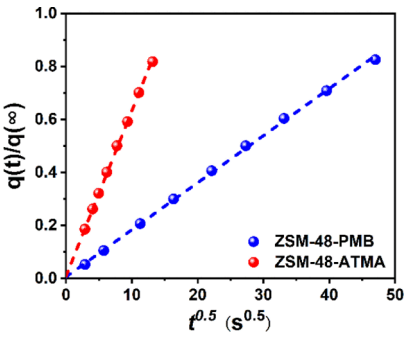

Figure 5. $2\text{-}MC_6$ adsorption rates in ZSM-48-PMB and ZSM-48-ATMA by fitting with eq 2.

https://dx.doi.org/10.1021/acs.iecr.0c00750
Ind. Eng. Chem. Res. 2020, 59, 11139−11148

Figures 1c and S5, show that ZSM-48-ATMA appears like a discrete rod, while ZSM-48-PMB has an intergrowth, branch-like structure. It is likely that the difference in diffusion property stems from varied morphological features in terms of aspect ratio and presence of grain boundaries. The isomer yield versus conversion curves, illustrating an overall effect, are depicted in Figure 4d, showing that the Pt/HZSM-48-ATMA catalyst gives a maximum isomer yield at 72% at a conversion of 78%, whereas a maximum yield from Pt/HZSM-48-PMB was 44% at a conversion of 66%. The product compositions at the maximum yield for each catalyst are exhibited in Table S4. MBs constitute the majority in isomers, except for the ethyl-branched isomer (less than 2.2%). For DBs, smaller DBs (i.e., 2,3-DMC_5 and 2,4-DMC_5) are preferentially produced over bulkier DBs (such as 2,2-DMC_5 and 3,3-DMC_5), suggesting that their formation is sterically limited within the narrow channels of the ZSM-48 crystal. The increasing order of DB product selectivity, that is, 3,3-DMC_5 < 2,2-DMC_5 < 2,4-DMC_5 < 2,3-DMC_5, is inversely proportional to the increasing order of their molecular size, reflecting a good measure of shape selectivity.[47] Both samples were catalytically stable for a time-on-stream of up to 72 h (Figure S10). In brief, ZSM-48-ATMA outperformed other microporous counterparts with a record high yield (as summarized in Table S5) owing to an increase in acid site density and a better diffusion property.

4. CONCLUSIONS

This work showcases a way to broaden the framework composition of zeolite, that is, the use of molecules mimicking reaction intermediates or transition states as OSDAs. This design concept presents a new opportunity to introduce structural and catalytic diversity in zeolitic materials and is potentially extendable. Because $ATMA^+$ is now a commodity monomer for the production of dispersants for drilling fluids, it is readily available and inexpensive. The synthetic exploration also suggests that the rigidity of OSDA endowed by the presence of a C═C double bond is a crucial factor that deserves further attention in future synthetic studies. A cost-effective method suitable to generate technologically important aluminous ZSM-48 possessing both high crystallinity and more acid site density is therefore established. Pt-loaded aluminous ZSM-48 exhibits high isomer yield in *n*-heptane hydroisomerization, thus proving the catalytic advantage in the pre-established catalytic reaction. It is believed that this simplified preparation and increased acidity in the obtained material would prompt the practical use of ZSM-48 zeolite and further broaden its applications.

■ ASSOCIATED CONTENT

Supporting Information

The Supporting Information is available free of charge at https://pubs.acs.org/doi/10.1021/acs.iecr.0c00750.

Structure-directing agents reported in literature; ^{13}C NMR spectra of home-made $PMBr_2$, ; TGA curves of as-synthesized zeolites; XRD patterns, field emission scanning electron micrographs, transmission electron micrographs, ^{27}Al MAS NMR spectra and ^{29}Si MAS NMR spectra; ^{27}Al isotropic chemical shift and quadrupolar parameters; Al−O−Si bond angle calculations; *n*-heptane conversion; product compositions and maximum isomer yields in catalytic tests (PDF)

■ AUTHOR INFORMATION

Corresponding Authors

Xiujie Li − *Dalian Institute of Chemical Physics, Chinese Academy of Sciences, Dalian 116023, P. R. China;* orcid.org/0000-0002-2649-4673; Email: xiujieli@dicp.ac.cn

Kake Zhu − *State Key Laboratory of Chemical Engineering, School of Chemical Engineering, East China University of Science and Technology, Shanghai 200237, P. R. China;* orcid.org/0000-0003-3071-0882; Email: kakezhu@ecust.edu.cn

Authors

Miao Zhai − *State Key Laboratory of Chemical Engineering, School of Chemical Engineering, East China University of Science and Technology, Shanghai 200237, P. R. China*

Hongxin Ding − *State Key Laboratory of Chemical Engineering, School of Chemical Engineering, East China University of Science and Technology, Shanghai 200237, P. R. China*

Shu Zeng − *Dalian Institute of Chemical Physics, Chinese Academy of Sciences, Dalian 116023, P. R. China*

Jiuxing Jiang − *MOE Key Laboratory of Bioinorganic and Synthetic Chemistry School of Chemistry, Sun Yat-sen University, Guangzhou 510275, P. R. China;* orcid.org/0000-0001-9664-3235

Shutao Xu − *Dalian Institute of Chemical Physics, Chinese Academy of Sciences, Dalian 116023, P. R. China;* orcid.org/0000-0003-4722-8371

Xinggui Zhou − *State Key Laboratory of Chemical Engineering, School of Chemical Engineering, East China University of Science and Technology, Shanghai 200237, P. R. China*

Complete contact information is available at: https://pubs.acs.org/10.1021/acs.iecr.0c00750

Author Contributions

‖M.Z. and H.D. contributed equally to the work.

Notes

The authors declare no competing financial interest.

■ ACKNOWLEDGMENTS

K.Z. is grateful for the financial support from National Natural Science Foundation of China (21878079). The authors thank the Research Center of Analysis and Test of East China University of Science and Technology for the help on the characterizations.

■ REFERENCES

(1) Davis, M. E.; Lobo, R. F. Zeolite and molecular sieve synthesis. *Chem. Mater.* **1992**, *4*, 756−768.

(2) Corma, A.; Davis, M. E. Issues in the synthesis of crystalline molecular sieves: towards the crystallization of low framework-density structures. *ChemPhysChem* **2004**, *5*, 304−313.

(3) Li, Y.; Yu, J. New stories of zeolite structures: their descriptions, determinations, predictions, and evaluations. *Chem. Rev.* **2014**, *114*, 7268−7316.

(4) Davis, M. E. Ordered porous materials for emerging applications. *Nature* **2002**, *417*, 813−821.

(5) Martínez, C.; Corma, A. Inorganic molecular sieves: Preparation, modification and industrial application in catalytic processes. *Coord. Chem. Rev.* **2011**, *255*, 1558−1580.

(6) Lobo, R. F.; Davis, M. E. CIT-1: A New Molecular Sieve with Intersecting Pores Bounded by 10- and 12-Rings. *J. Am. Chem. Soc.* **1995**, *117*, 3766−3779.

(7) Corma, A.; Rey, F.; Rius, J.; Sabater, M. J.; Valencia, S. Supramolecular self-assembled molecules as organic directing agent for synthesis of zeolites. *Nature* **2004**, *431*, 287−290.
(8) Boal, B. W.; Schmidt, J. E.; Deimund, M. A.; Deem, M. W.; Henling, L. M.; Brand, S. K.; Zones, S. I.; Davis, M. E. Facile Synthesis and Catalysis of Pure-Silica and Heteroatom LTA. *Chem. Mater.* **2015**, *27*, 7774−7779.
(9) Ryu, T.; Ahn, N. H.; Seo, S.; Cho, J.; Kim, H.; Jo, D.; Park, G. T.; Kim, P. S.; Kim, C. H.; Bruce, E. L.; Wright, P. A.; Nam, I.-S.; Hong, S. B. Fully Copper-Exchanged High-Silica LTA Zeolites as Unrivaled Hydrothermally Stable NH_3-SCR Catalysts. *Angew. Chem., Int. Ed.* **2017**, *56*, 3256−3260.
(10) Gallego, E. M.; Portilla, M. T.; Paris, C.; León-Escamilla, A.; Boronat, M.; Moliner, M.; Corma, A. "Ab initio" synthesis of zeolites for preestablished catalytic reactions. *Science* **2017**, *355*, 1051−1054.
(11) Li, C.; Paris, C.; Martínez-Triguero, J.; Boronat, M.; Moliner, M.; Corma, A. Synthesis of reaction-adapted zeolites as methanol-to-olefins catalysts with mimics of reaction intermediates as organic structure-directing agents. *Nat. Catal.* **2018**, *1*, 547−554.
(12) Chu, P. Deptford, Silico-Crystal Method of Preparing Same and Catalytic Conversion Therewith. U.S. Patent 4,397,827 A, August 9, 1983.
(13) Lobo, R. F.; van Koningsveld, H. New Description of the Disorder in Zeolite ZSM-48. *J. Am. Chem. Soc.* **2002**, *124*, 13222−13230.
(14) Lee, S.-H.; Shin, C.-H.; Yang, D.-K.; Ahn, S.-D.; Nam, I.-S.; Hong, S. B. Reinvestigation into the synthesis of zeolites using diquaternary alkylammonium ions $(CH_3)_3N^+(CH_2)_nN^+(CH_3)_3$ with n = 3-10 as structure-directing agents. *Microporous Mesoporous Mater.* **2004**, *68*, 97−104.
(15) Astafan, A.; Benghalem, M. A.; Michelin, L.; Rigolet, S.; Patarin, J.; Pinard, L.; Daou, T. J. Synthesis of hierarchical ZSM-48 nanozeolites. *New J. Chem.* **2018**, *42*, 4457−4464.
(16) Martens, J. A.; Parton, R.; Uytterhoeven, L.; Jacobs, P. A.; Froment, G. F. Selective conversion of decane into branched isomers: a comparison of platinum/ZSM-22, platinum/ZSM-5 and platinum/USY zeolite catalysts. *Appl. Catal.* **1991**, *76*, 95−116.
(17) Claude, M. C.; Martens, J. A. Monomethyl-Branching of Long n-Alkanes in the Range from Decane to Tetracosane on Pt/H-ZSM-22 Bifunctional Catalyst. *J. Catal.* **2000**, *190*, 39−48.
(18) Arroyo, J. A. M.; Martens, G. G.; Froment, G. F.; Marin, G. B.; Jacobs, P. A.; Martens, J. A. Hydrocracking and isomerization of n-paraffin mixtures and a hydrotreated gasoil on Pt/ZSM-22: Confirmation of pore mouth and key-lock catalysis in liquid phase. *Appl. Catal. A* **2000**, *192*, 9−22.
(19) Huybrechts, W.; Vanbutsele, G.; Houthoofd, K. J.; Bertinchamps, F.; Laxmi Narasimhan, C. S.; Gaigneaux, E. M.; Thybaut, J. W.; Marin, G. B.; Denayer, J. F. M.; Baron, G. V.; Jacobs, P. A.; Martens, J. A. Skeletal isomerization of octadecane on bifunctional ZSM-23 zeolite catalyst. *Catal. Lett.* **2005**, *100*, 235−242.
(20) Molino, A.; Łukaszuk, K. A.; Rojo-Gama, D.; Lillerud, K. P.; Olsbye, U.; Bordiga, S.; Svelle, S.; Beato, P. Conversion of methanol to hydrocarbons over zeolite ZSM-23 (MTT): exceptional effects of particle size on catalyst lifetime. *Chem. Commun.* **2017**, *53*, 6816−6819.
(21) Chen, Y.; Li, C.; Chen, X.; Liu, Y.; Liang, C. Synthesis of ZSM-23 zeolite with dual structure directing agents for hydroisomerization of n-hexadecane. *Microporous Mesoporous Mater.* **2018**, *268*, 216−224.
(22) Mériaudeau, P.; Tuan, V. A.; Nghiem, V. T.; Sapaly, G.; Naccache, C. Comparative evaluation of the catalytic properties of SAPO-31 and ZSM-48 for the hydroisomerization of n-octane: effect of the acidity. *J. Catal.* **1999**, *185*, 435−444.
(23) Kim, J.; Han, S. W.; Kim, J.-C.; Ryoo, R. Supporting Nickel To Replace Platinum on Zeolite Nanosponges for Catalytic Hydroisomerization of n-Dodecane. *ACS Catal.* **2018**, *8*, 10545−10554.
(24) Ahmed, M. H. M.; Muraza, O.; Nakaoka, S.; Jamil, A. K.; Mayoral, A.; Sebastian, V.; Yamani, Z. H.; Masuda, T. Stability Assessment of Regenerated Hierarchical ZSM-48 Zeolite Designed by Post-Synthesis Treatment for Catalytic Cracking of Light Naphtha. *Energy Fuels* **2017**, *31*, 14097−14103.
(25) Zhang, M.; Li, C.; Chen, X.; Chen, Y.; Liang, C. Hierarchical ZSM-48-Supported Nickel Catalysts with Enhanced Hydroisomerization Performance of Hexadecane. *Ind. Eng. Chem. Res.* **2019**, *58*, 19855−19861.
(26) Kim, W.; Kim, J.-C.; Kim, J.; Seo, Y.; Ryoo, R. External Surface Catalytic Sites of Surfactant-Tailored Nanomorphic Zeolites for Benzene Isopropylation to Cumene. *ACS Catal.* **2013**, *3*, 192−195.
(27) Teketel, S.; Skistad, W.; Benard, S.; Olsbye, U.; Lillerud, K. P.; Beato, P.; Svelle, S. Shape Selectivity in the Conversion of Methanol to Hydrocarbons: The Catalytic Performance of One-Dimensional 10-Ring Zeolites: ZSM-22, ZSM-23, ZSM-48, and EU-1. *ACS Catal.* **2012**, *2*, 26−37.
(28) Zhang, M.; Wang, L.; Chen, Y.; Zhang, Q.; Liang, C. Creating mesopores in ZSM-48 zeolite by alkali treatment: Enhanced catalyst for hydroisomerization of hexadecane. *J. Energ. Chem.* **2016**, *25*, 539−544.
(29) Weisz, P. B.; Swegler, E. W. Stepwise reaction on separate catalytic centers: isomerization of saturated hydrocarbons. *Science* **1957**, *126*, 31−32.
(30) Guisnet, M. "Ideal" bifunctional catalysis over Pt-acid zeolites. *Catal. Today* **2013**, *218*−*219*, 123−134.
(31) Noh, G.; Shi, Z.; Zones, S. I.; Iglesia, E. Isomerization and β-scission reactions of alkanes on bifunctional metal-acid catalysts: Consequences of confinement and diffusional constraints on reactivity and selectivity. *J. Catal.* **2018**, *368*, 389−410.
(32) Zhai, M.; Li, L.; Ba, Y.; Zhu, K.; Zhou, X. Fabricating ZSM-23 with reduced aspect ratio through ball-milling and recrystallization: Synthesis, structure and catalytic performance in N-heptane hydroisomerization. *Catal. Today* **2019**, *329*, 82−93.
(33) Emeis, C. A. Determination of integrated molar extinction coefficients for infrared absorption bands of pyridine adsorbed on solid acid catalysts. *J. Catal.* **1993**, *141*, 347−354.
(34) Taouli, A.; Klemt, A.; Breede, M.; Reschetilowski, W. Acidity investigations and determination of integrated molar extinction coefficients for infrared absorption bands of ammonia adsorbed on acidic sites of MCM-41. *Stud. Surf. Sci. Catal.* **1999**, *125*, 307−314.
(35) Barzetti, T.; Selli, E.; Moscotti, D.; Forni, L. Pyridine and ammonia as probes for FTIR analysis of solid acid catalysts. *Faraday Trans.* **1996**, *92*, 1401−1407.
(36) Su, X.; Xu, S.; Tian, P.; Li, J.; Zheng, A.; Wang, Q.; Yang, M.; Wei, Y.; Deng, F.; Liu, Z. Investigation of the Strong Bronsted Acidity in a Novel SAPO-type Molecular Sieve, DNL-6. *J. Phys. Chem. C* **2015**, *119*, 2589−2596.
(37) Kim, M. Y.; Lee, K.; Choi, M. Cooperative effects of secondary mesoporosity and acid site location in Pt/SAPO-11 on n-dodecane hydroisomerization selectivity. *J. Catal.* **2014**, *319*, 232−238.
(38) Lippmaa, E.; Samoson, A.; Magi, M. High-Resolution ^{27}NMR of aluminosilicates. *J. Am. Chem. Soc.* **1986**, *108*, 1730−1735.
(39) Samoson, A.; Lippmaa, E.; Engelhardt, G.; Lohse, U.; Jerschkewitz, H.-G. Quantitative high-resolution ^{27}Al NMR: tetrahedral non-framework aluminum in hydrothermally treated zeolites. *Chem. Phys. Lett.* **1987**, *134*, 589−592.
(40) Kim, S.; Park, G.; Woo, M. H.; Kwak, G.; Kim, S. K. Control of Hierarchical Structure and Framework-Al Distribution of ZSM-5 via Adjusting Crystallization Temperature and Their Effects on Methanol Conversion. *ACS Catal.* **2019**, *9*, 2880−2892.
(41) Wan, Z.; Wu, W.; Chen, W.; Yang, H.; Zhang, D. Direct Synthesis of Hierarchical ZSM-5 Zeolite and Its Performance in Catalyzing Methanol to Gasoline Conversion. *Ind. Eng. Chem. Res.* **2014**, *53*, 19471−19478.
(42) Bräuer, P.; Ng, P. L.; Situmorang, O.; Hitchcock, I.; D'Agostino, C. Effect of Al content on number and location of hydroxyl acid species in zeolites: a DRIFTS quantitative protocol without the need for molar extinction coefficients. *RSC Adv.* **2017**, *7*, 52604−52613.
(43) Yang, L.; Wang, W.; Song, X.; Bai, X.; Feng, Z.; Liu, T.; Wu, W. The hydroisomerization of n-decane over Pd/SAPO-11 bifunctional

https://dx.doi.org/10.1021/acs.iecr.0c00750
Ind. Eng. Chem. Res. 2020, 59, 11139−11148

catalysts: The effects of templates on characteristics and catalytic performances. *Fuel Process. Technol.* **2019**, *190*, 13−20.
(44) Jin, D.; Ye, G.; Zheng, J.; Yang, W.; Zhu, K.; Coppens, M.-O.; Zhou, X. Hierarchical Silicoaluminophosphate Catalysts with Enhanced Hydroisomerization Selectivity by Directing the Orientated Assembly of Premanufactured Building Blocks. *ACS Catal.* **2017**, *7*, 5887−5902.
(45) Yue, T.; Liu, W.; Li, L.; Zhao, X.; Zhu, K.; Zhou, X.; Yang, W. Crystallization of ATO silicoaluminophosphates nanocrystalline spheroids using a phase-transfer synthetic strategy for n-heptane hydroisomerization. *J. Catal.* **2018**, *364*, 308−327.
(46) Kim, J.; Kim, W.; Seo, Y.; Kim, J.-C.; Ryoo, R. n-Heptane hydroisomerization over Pt/MFI zeolite nanosheets: Effects of zeolite crystal thickness and platinum location. *J. Catal.* **2013**, *301*, 187−197.
(47) Raybaud, P.; Patrigeon, A.; Toulhoat, H. The origin of the C_7-hydroconversion selectivities on Y, *β*, ZSM-22, ZSM-23, and EU-1 zeolites. *J. Catal.* **2001**, *197*, 98−112.

https://dx.doi.org/10.1021/acs.iecr.0c00750
Ind. Eng. Chem. Res. 2020, 59, 11139−11148